ARTICLE Open Access

Vectorial lasing with designable topological charges based on Möbius-like correspondence in quasi-BICs

Xinhao Wang[1], Zhaochen Wu[1], Jiajun Wang[1,2,3]✉, Lei Shi[1,2,3,4,5]✉ and Jian Zi[1,2,3,4,5]✉

Abstract

The ability to control topological properties of laser emission represents a fundamental advancement in photonic technology. Achieving topological lasing in a single compact photonic structure is crucial for device integration and miniaturization, but faces significant challenges for designing both the high-quality (high-Q) mode and radiative topological configurations. Recently, bound states in the continuum (BICs), as extraordinary states possessing both ultrahigh Q factors and polarization topological charges, have been demonstrated as a promising platform for compact topological lasing. However, as the cornerstone of BIC lasing's non-trivial properties, topological charges of BICs are protected by real-space structural symmetries, which simultaneously impose fundamental limitations that hinder the designability of lasing topological charges. Here, we propose and experimentally demonstrate a compound cavity design method based on the Möbius-like correspondence in quasi-BICs (q-BICs), by which compact vectorial lasing with designable topological charges can be realized. We reveal the hidden connection between real-space symmetry breaking and eigen-polarizations of q-BICs from the triangular photonic crystal (PhC) slab, manifesting as a Möbius-like correspondence. By splicing PhC slab sectors utilizing this Möbius-like correspondence, we establish a one-to-one correspondence between compound cavities and their lasing topological charges. Vectorial lasing with designable topological charges from −5 to +5 was experimentally realized. Our work establishes a novel BIC-based platform that enables designable topological lasing, providing a promising route toward compact topological sources.

Introduction

The presence of non-trivial topological structures in lasing profiles endows optical fields with rich properties and functionalities[1–7], enabling many applications from metrology[8], microscopy[9,10], optical manipulation to quantum information processing[11–13] and light-matter interactions[14,15], etc. Directly implementing lasing with non-trivial topological structures through single compact photonic structures represents a highly desirable yet challenging goal in modern optics, as it would substantially advance the integration and miniaturization of photonic devices while maintaining their complex functionalities. Progress has been made through various approaches like Dirac-vortex cavities[16–19], photonic disclination cavities[20,21], compound cavities with metasurfaces[22–24] and other topological mode cavities[25], etc[26–28]; yet, substantial challenges persist in achieving non-trivial lasing profiles with designability of the topological charges and single-compact-structure implementation. For instance, while Dirac-vortex cavities have demonstrated the possibility of vectorial lasing with polarization topological charges through topological mid-gap modes, the correspondence between cavity structures and topological charges remains ambiguous[16]. Meanwhile, conventional resonant metasurfaces, limited by their lack of high-quality (high-Q) modes, typically require additional cavities to achieve topological charge lasing[22–24]. For most existing topological lasing based on cavity modes, the achievable topological charges are

Correspondence: Jiajun Wang (jiajunwang@fudan.edu.cn) or
Lei Shi (lshi@fudan.edu.cn) or Jian Zi (jzi@fudan.edu.cn)
[1]State Key Laboratory of Surface Physics, Key Laboratory of Micro- and Nano-Photonic Structures (Ministry of Education) and Department of Physics, Fudan University, 200433 Shanghai, China
[2]Shanghai Research Center for Quantum Sciences, 201315 Shanghai, China
Full list of author information is available at the end of the article
These authors contributed equally: Xinhao Wang, Zhaochen Wu, Jiajun Wang

© The Author(s) 2026
Open Access This article is licensed under a Creative Commons Attribution 4.0 International License, which permits use, sharing, adaptation, distribution and reproduction in any medium or format, as long as you give appropriate credit to the original author(s) and the source, provide a link to the Creative Commons licence, and indicate if changes were made. The images or other third party material in this article are included in the article's Creative Commons licence, unless indicated otherwise in a credit line to the material. If material is not included in the article's Creative Commons licence and your intended use is not permitted by statutory regulation or exceeds the permitted use, you will need to obtain permission directly from the copyright holder. To view a copy of this licence, visit http://creativecommons.org/licenses/by/4.0/.

typically determined through numerical calculation after cavity design, making the purposeful design of desired topological charges particularly challenging, with realized topological charges confined to low orders. These limitations not only point to further directions for those research areas but also highlight the crucial requirements for exploring novel design methods of compact topological lasing.

In the exploration of novel topological lasing designs, bound states in the continuum (BICs) have emerged as a promising platform due to their unique properties revealed in recent studies of topological photonics[29–32]. BICs have been found to exhibit unexpected polarization vortices in momentum space, offering vectorial topological configurations in photonic bands[33–35]. These counterintuitive momentum-space vortices are supported by real-space periodic structures like photonic crystal (PhC) slabs, manifesting as winding polarization states of eigen optical modes surrounding BICs, and have been applied in resonant systems to generate light fields with non-trivial characteristics[36–38]. By accumulating the winding angle in polarization vortices, quantized numbers can be defined as topological charges of BICs[29]. The non-trivial topological configurations of BICs also enable another prominent property, i.e., infinite Q factors, which has driven their widespread application in nonlinear optics and light–matter interaction, including high-efficiency high-harmonic generation[39–43], Bose–Einstein condensation[44,45] and compact lasing platforms[46,47]. In particular, in BIC-based lasing systems, the intrinsic momentum-space topology can be transferred into the emitted optical fields, enabling the realization of vectorial lasing modes with topological charges[48–52].

Microlaser design based on the BIC concept represents a highly valuable method for compact topological lasing. The non-trivial lasing profiles are dominated by momentum-space topological vortex configurations of BICs, which are protected by real-space structural symmetries[29,32]. However, these symmetries fundamentally constrain the allowable topological charges of BICs, as only specific vortex configurations are permitted under given symmetry operations. This restriction on topological charges consequently limits the controllability and designability of current BIC-based microlaser systems. Breaking the original structures' symmetry is necessary for the goal of purposefully designing different topological charges. While, the fundamental inquiry of how to construct topological lasing modes from symmetry-breaking BIC systems remains largely unexplored.

In this work, we introduce a compound cavity design strategy for realizing vectorial lasing with designable topological charges by leveraging Möbius-like correspondence in quasi-BICs (q-BICs). Here, q-BICs are high-Q optical modes that arise from symmetry-protected BICs through slight symmetry breaking, with their eigenpolarizations intrinsically linked to the symmetry-breaking parameters. We explored the hidden connection between structural symmetry breaking and eigen-polarizations of q-BICs from a high-order BIC with -2 topological charge in the triangular PhC slab, which manifests as a Möbius-like correspondence. Guided by this correspondence, multiple q-BIC PhC slabs with distinct structural parameters and eigen-polarizations are spliced in an ordered angular sequence to form compound cavities supporting vectorial topological lasing modes. This cavity construction concept, based on Möbius-like correspondence, establishes a one-to-one correspondence between cavity configuration and lasing topological charge. Experimentally, vectorial lasing with designable topological charges ranging from -5 to $+5$ was realized.

Results

Concept

To introduce the basic concept, we begin with the continuous evolution of q-BICs under symmetry-breaking parameter manipulation. The first column of Fig. 1b shows the top view of a triangular-lattice PhC slab and the corresponding polarization distribution in momentum space in a photonic band. A symmetry-protected BIC is located at the momentum-space center (Γ point). With C_6 rotational symmetry, the BIC is enabled with a topological charge of -2. When slightly breaking the C_6 symmetry to C_2 symmetry via changing the circular holes to be elliptic holes, momentum-space polarization configurations vary and at Γ point the BIC evolves to a q-BIC[41,53]. Under slight symmetry breaking, the at-Γ q-BIC still has a high Q factor and carries linear polarization[41,54,55]. The orientation of linear polarization in momentum space (φ in Fig. 1c) shows a close connection with the symmetry breaking, more precisely, the orientation of elliptic holes in real space (θ in Fig. 1c). The q-BIC's polarization orientation φ rotates continuously along with the symmetry breaking orientation θ, as shown in Fig. 1b. Notably, in the second and fourth columns of Fig. 1b, we can see two types of PhC slabs with different symmetry breaking orientation θ can have q-BICs with the same polarization orientation φ. The continuous parameter relationship between the real-space symmetry-breaking structure and the eigen-polarization of its supported q-BIC can be represented by the Möbius-like correspondence shown in Fig. 1c. As the angle θ evolves from 0 to π, the q-BIC's polarization orientation φ undergoes a complete cycle of 2π, which can be described as a closed loop on the Möbius strip.

In short, the Möbius-like correspondence between the structural symmetry breaking and eigen-polarization of q-BIC establishes a foundational framework for achieving designable topological charges with a compound cavity. Based on the elucidated design and functionality

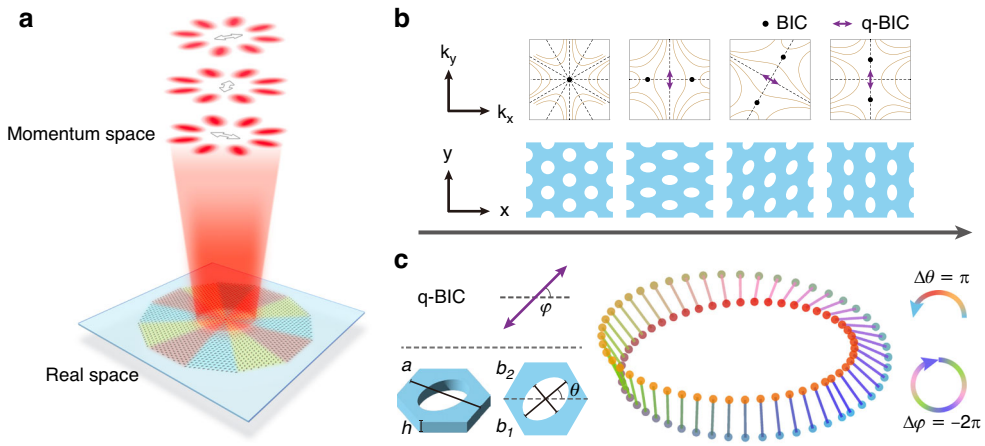

Fig. 1 Principle of the vectorial lasing with designable topological charge. **a** Schematic of a vectorial lasing with −4 topological charge. The cavity is constructed by arranging three types of PhC slabs which support q-BICs of different eigen-polarizations. **b** Schematic, relationship between momentum-space polarization configurations and PhC structures. The lower panel shows a top view of the PhC slabs. The upper panel shows the corresponding polarization distribution, in which dashed lines mark the mirror planes, and the solid lines represent the continuous evolution of the major axes of the eigen-polarization states across different optical modes. **c** Left panel, definition of the polarization orientation of q-BIC (φ, ranging from $-\pi/2$ to $\pi/2$) and the rotation angle of the elliptical hole (θ, ranging from 0 to π). Right panel, the correspondence between the PhC and q-BIC manifests as a Möbius-strip-like representation. The spheres embedded at the edge of the Möbius strip refer to PhC of different rotation angle θ, and the surface of the Möbius strip (the lines between the two spheres) refers to the polarization orientation φ of the q-BIC. As θ evolves from 0 to π clockwise or counterclockwise ($|\Delta\theta| = \pi$), the corresponding q-BIC completes a closed loop (two polarization cycles) along the edge of the Möbius strip ($|\Delta\varphi| = 2\pi$)

precursor in Fig. 1b, c, the general methodology for realizing vectorial lasing with designable topological charge was schematically illustrated in Fig. 1a. The compound cavity is constructed by splicing different regions of PhC designs on a single slab, with a definite structural center. These colored PhC slabs, all sharing the same triangular lattice, are modified in terms of the orientations of the elliptical holes to support q-BICs with distinct linear polarizations. The arrangement principle is based on the polarization continuity enabled by the Möbius-like correspondence, to finally form a compound cavity supporting a topological charge lasing mode. By intentionally designing the interior arrangement for the compound cavity, we can purposefully control the absolute value and sign of the lasing topological charge.

Experimental realization

To directly demonstrate the Möbius-like correspondence in q-BICs, we performed lasing experiments via PhC slabs with different symmetry-breaking parameters. The designed PhC slabs are fabricated by etching periodic elliptical holes in a silicon nitride (Si_3N_4, refractive index ~2) film on the optical silica substrate, with the unit cell shown in Fig. 1c. The lattice constant a is 634 nm, and Si_3N_4 thickness t is 140 nm. For the etched elliptical holes, the major/minor axis lengths are fixed at $b_1 = 480$ nm and $b_2 = 320$ nm.

To give a specific example in detail, we simulated and experimentally characterized one PhC slab ($\theta = 0°$). In simulations, the PhC slabs are embodied in the optical silica environment (refractive index ~1.45). For practical experiments, PhC slabs are immersed in dimethyl sulfoxide (DMSO) to match the refractive index of optical silica. As shown in Supplementary Information Section 4, we first analyzed the designed photonic band (blue color) and the momentum-space properties. In this case, the at-Γ q-BIC carries a y-direction eigen polarization ($\varphi = 90°$) and has a high Q factor. This designed PhC slab was fabricated by the electron beam lithography process, and Fig. 2a shows the corresponding scanning electron microscopy (SEM) image. The photonic band and q-BIC are directly observed and characterized by the polarization-analyzed momentum-space spectroscopy measurement system, as shown in Supplementary Information Section 4. To achieve q-BIC lasing, IR-140 dye molecules were chosen as the gain medium and were dissolved in DMSO, overlaid on the PhC slabs. A femtosecond pulse laser was applied as the pumping source to validate the q-BIC lasing behaviors. Detailed fabrication and optical measurement procedures are provided in "Materials and methods" and Supplementary Information Section 2 and 3.

Figure 2b displays the normalized photoluminescence (PL) spectra at varying pump intensities, clearly revealing a phase transition from spontaneous emission to lasing emission. The corresponding light-light curve and linewidth evolution curve are extracted from the PL spectra, as shown in Fig. 2c. The observed S-shaped curve and

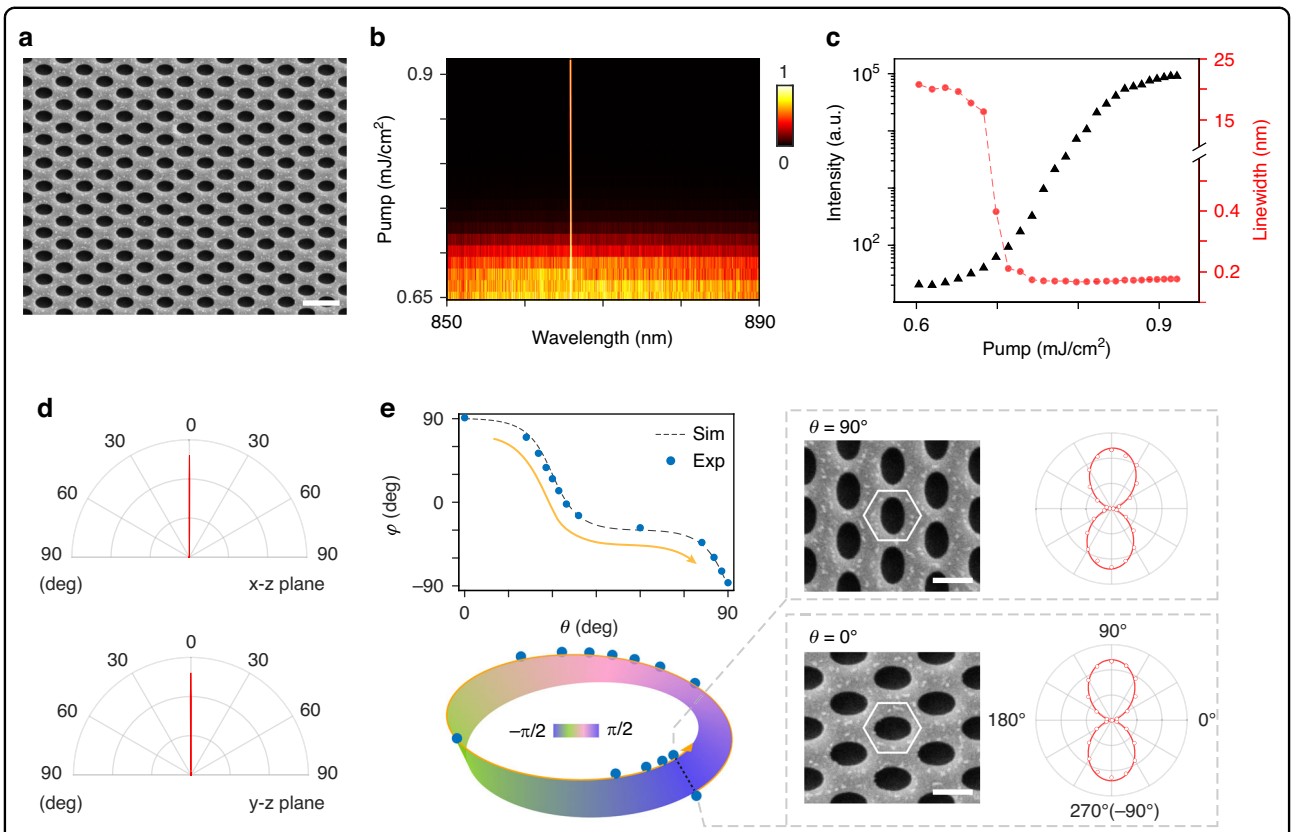

Fig. 2 Lasing properties via q-BIC and measured Möbius-like correspondence. a SEM images of the fabricated PhC slab with $\theta = 0°$. Scale bar, 1 μm. **b** Normalized PL spectra at varying pump intensity. **c** Light–light curve (in black) and linewidth evolution curve (in red) as functions of pump intensity for the lasing mode. **d** Measured directivity of the emission above the lasing threshold in x-z and y-z planes. **e** Left, lasing emission polarizations φ measured as a function of the structural parameter θ. Experimental results (blue circles) show good agreement with the simulated polarization of the quasi-BIC (gray dashed line) in the upper panel, confirming the Möbius-like correspondence (bottom). The color of the Möbius strip describes the polarization orientation φ. Right, SEM images and experimentally measured lasing emission polarizations of the PhC slab with $\theta = 0°$ (top) and $\theta = 90°$ (bottom), corresponding to the two endpoints of a tangent line on the Möbius strip (black dashed line). Scale bar, 500 nm

dramatic reduction in linewidth are characteristic of lasing threshold behavior, further confirming the transition to lasing emission. Above the threshold, the lasing emission matches the q-BIC mode both in wavelength and radiation direction. As shown in Fig. 2d, the lasing emission exhibits high directivity along the z-axis (normal direction, corresponding to the Γ point in momentum space) with radiation angles of ±0.6° in the x-z plane and ±0.8° in the y-z plane, validating the q-BIC lasing. The lower right panel of Fig. 2e exhibits the measured polarization of the q-BIC lasing ($\varphi = 90°$), agreeing well with the linear polarization in the simulation.

A series of the PhC slabs with different rotation angles θ was further fabricated to directly map the Möbius-like correspondence between eigen-polarizations of q-BICs and the structural symmetry breaking via the lasing measurements. We measured their emission polarization orientations above threshold and plotted them as a function of θ in the upper left panel of Fig. 2e. Detailed SEM images and measured lasing emission polarizations are shown in the right panels of Fig. 2e and Supplementary Information Section 6. The experimental data align well with the simulations and exhibit a Möbius-like correspondence (left panel of Fig. 2e) following the principles introduced in Fig. 1c. As indicated by the orange arrows, the experimental results trace half the path along the edge of the Möbius strip, achieving full linear polarization coverage on the equator of the Poincaré sphere. Notably, for PhC slabs of $\theta = 0°$ and 90°, their polarization orientations coincide and are located at the two endpoints of a tangent line (black dashed line), embodying the Möbius-like correspondence in q-BICs. Exploiting the mirror symmetry of the structures, the remaining half path can be extrapolated from the current results, together forming a complete Möbius-like correspondence in Fig. 1c. Meanwhile, the eigen-frequency of the q-BIC exhibits only minor variations, as shown in Supplementary Information Section 5.

With the Möbius-like correspondence, we demonstrated the construction method of compound cavities supporting vectorial lasing mode with designable topological charges. To clarify the general design principle of lasing topological

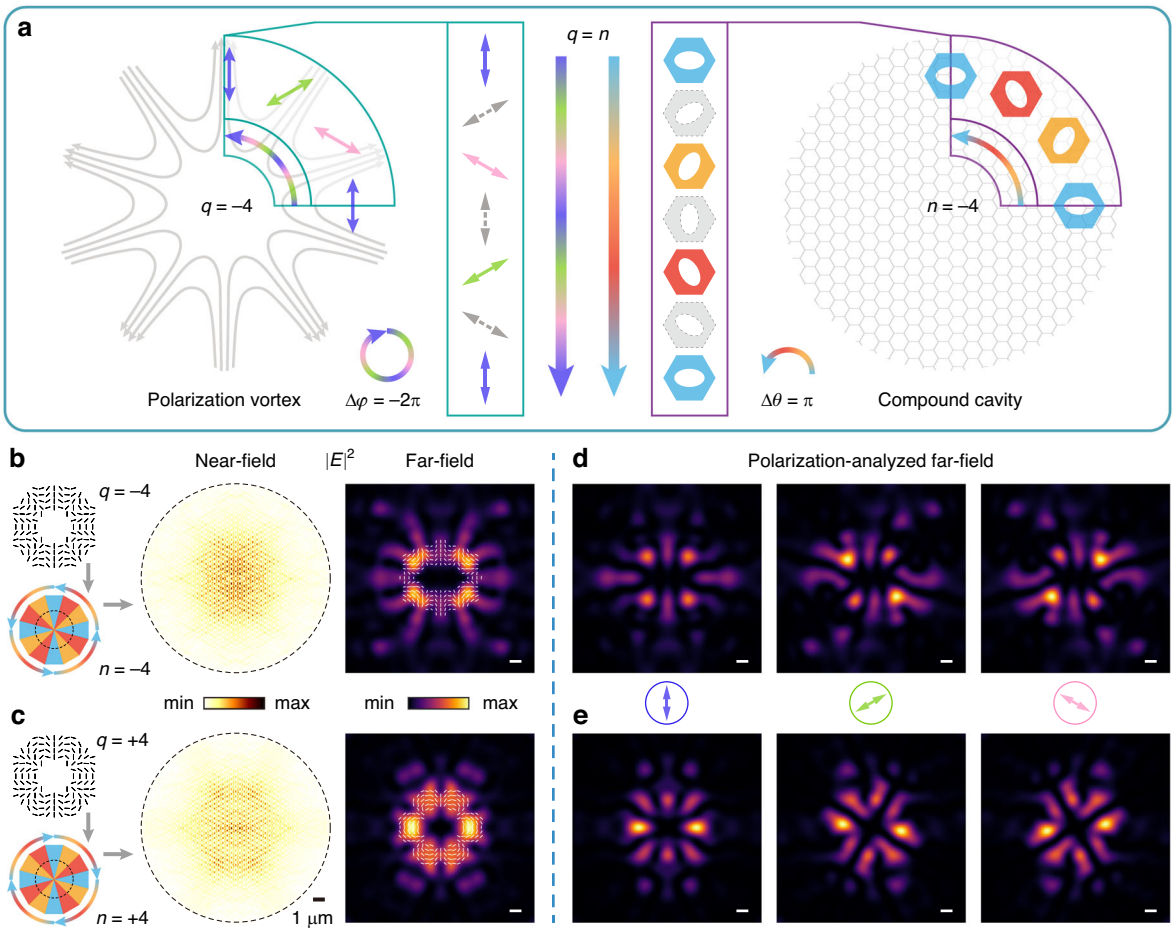

Fig. 3 Construction of compound cavities based on Möbius-like correspondence. **a** Schematic of the construction principle. Left, illustration of the polarization vortex with −4 topological charge. Right, schematic of the constructed compound cavity consisting of angularly repeating sections. The repeating section is composed of three types of q-BIC PhC slabs with $\theta = 0°$ (blue), 60° (yellow), and 120° (orange). The middle panel shows the Möbius-like correspondence, where gray dashed polarizations and unit cells of PhC are plotted to show the intermediate parts along the minimum parameter path. **b**, **c** Construction of compound cavities for vectorial lasing with topological charges of −4 (**b**) and +4 (**c**). Left: schematic of the targeted polarization vortices and corresponding cavity design. Right: simulated near-field and far-field profiles of the cavity modes. The far-field polarization major axis distributions agree well with the targeted polarization vortices. Scale bar, 1°. **d**, **e** Simulated polarization-analyzed far-field profiles of the cavity modes $q = -4$ (**d**) and $q = +4$ (**e**). Colored arrows denote the analyzed polarization directions. Scale bar, 1°

charge, we begin with the example of a vectorial lasing mode with a topological charge of −4, as illustrated in Fig. 3a. The topological charge is characterized by the far-field polarization vector distribution, which exhibits a vortex configuration with a singularity at the center.

Specifically, the topological charge q is determined by the total winding angle of the polarization orientation φ along a closed loop traced in the counterclockwise direction:

$$q = \frac{1}{2\pi}\oint_c \frac{\partial\varphi}{\partial\psi}\mathrm{d}\psi \tag{1}$$

Here, ψ denotes the azimuthal angle within the two-dimensional plane of the vortex. From previous results, we can see the elliptic hole's rotation of π refers to a polarization winding of 2π in the discovered Möbius-like correspondence, reflecting an absolute topological charge of 1, while the sign of the topological charge can be controlled by adjusting the direction of the polarization rotation. Then, for the considered vectorial lasing mode with −4 topological charge (left panel in Fig. 3a), the polarization distribution can be decomposed into four angularly arranged repeating sections, each contributing a topological charge of −1 and highlighted by a cyan sector. Guided by the Möbius-like correspondence shown in the middle panel of Fig. 3a, we translate the targeted polarization states (left panel) into the structural parameters of q-BIC PhC sections in real-space counterparts (right panel). To support the targeted topological

polarization vortex distribution, three types of q-BIC PhC slabs, each with a different rotation angle, are arranged along the angular direction to form the real-space repeating section, highlighted by the purple sector (right panel in Fig. 3a). With the consideration for the minimum path of the Möbius-like correspondence, just three types of PhC slabs can ensure the required polarization variations in the designed structure. In the middle panel, gray dashed arrows and hexagons indicate the intermediate q-BIC polarizations and PhC unit cells along the minimal path on the Möbius-like correspondence.

Once the repeating section is established, constructing topological charges becomes straightforward. By angularly repeating the real-space section n times, a compound cavity is formed that supports a vectorial lasing mode carrying the targeted polarization vortex with topological charge q. The sign of topological charge can be controlled by the angular arrangement of PhC slabs: clockwise assembly yields positive q while counterclockwise assembly yields negative q. For clarity, we define the sign of the repetition number n to indicate the arrangement direction, with $n > 0$ corresponding to clockwise and $n < 0$ to counterclockwise. Consequently, our construction method exhibits a unique feature: a one-to-one correspondence between the compound cavities and their lasing topological charges, explicitly given by

$$n = q \tag{2}$$

To validate the construction strategy for the compound cavity, we further consider the cases of topological charges -4 and $+4$. Starting from the targeted topological charges of the nontrivial polarization distributions, as shown in the left panels of Fig. 3b, c, two compound cavities were accordingly designed by angularly repeating the real-space sections -4 and $+4$ times, respectively. The angular arrangement of the q-BIC PhC slabs constructs a compound cavity and supports a cavity mode localized at the structure center for vectorial lasing, as confirmed by the simulated near-field profiles in the right panels of Fig. 3b, c. These modes carry polarization vortices in the far field, where the extracted polarization major axis distributions agree well with the targeted topological polarization vortex configurations. Under linear polarization analysis, eight nodes appear in the polarization-analyzed far-field patterns of Fig. 3d, e, rotating in the opposite and same directions to the linear polarizer for the cases of topological charges $q = -4$ and $q = +4$, respectively, in agreement with the expected polarization distributions. More details about the simulations of the field profiles are provided in "Materials and Methods" and Supplementary Information Section 1.

Following the structural design in Fig. 3b, c, we experimentally fabricated the compound cavities to realize corresponding vectorial lasing. Figure 4a, c show the SEM images of the fabricated structures supporting vectorial lasing with topological charge of -4 and $+4$, respectively, where different colors highlight the rotation orientations of the elliptic holes in q-BIC PhC slabs. The color definitions on the structures are detailed in Fig. 4b, consistent with the schematic representation in Fig. 3a. With optical pumping focused on the structure's center, we experimentally realized the vectorial lasing with targeted topological charge. Figure 4d, e exhibit the measured lasing profiles in the far field. The polarization-analyzed images directly reveal the topological charges of lasing profiles, showing agreement with the simulated far-field profiles in Fig. 3d, e.

Finally, Fig. 5 further expands on our findings, showcasing the experimental realization of various vectorial lasing with different topological charges based on the proposed method. Figure 5a, b present measured total lasing profiles with topological charges ranging from -1 to -3, -5, $+1$ to $+3$, and $+5$. Detailed structural designs are presented in Supplementary Information Section 7. The polarization-analyzed lasing images are provided in Supplementary Information Section 8 in detail, reinforcing the controllability and designability of our approach to generate vectorial lasing with a range of topological charges. More characteristics of the emitted vectorial lasing are analyzed and compared in detail in Supplementary Information Section 9.

Discussion

Our work introduces a new paradigm for realizing vectorial lasing with designable topological charges by exploiting the Möbius-like correspondence in q-BICs. This approach is fundamentally distinct from conventional BIC-based lasing, where vectorial lasing relies on the intrinsic topological vortex configurations of symmetry-protected BICs—a mechanism inherently constrained by structural symmetries, thus limiting the designability of topological charges (see Supplementary Information Section 12). In contrast, we propose first breaking the original structural symmetry to obtain PhC slabs supporting q-BICs, and then constructing new compound cavities using these q-BIC PhC slabs. The absolute value and sign of the lasing topological charges are determined by the repetition times and the direction of the angular arrangement of the q-BIC PhC sectors, enabling highly flexible design of integer-order topological charges. Note that the topological polarization configurations are not formed by the direct interference of individual q-BIC lasing modes. When the compound-cavity configuration is modified to disrupt the original angular repetition based on the Möbius-like correspondence, the lasing behaviors will not be intuitively predictable. Additional experimental results and discussions

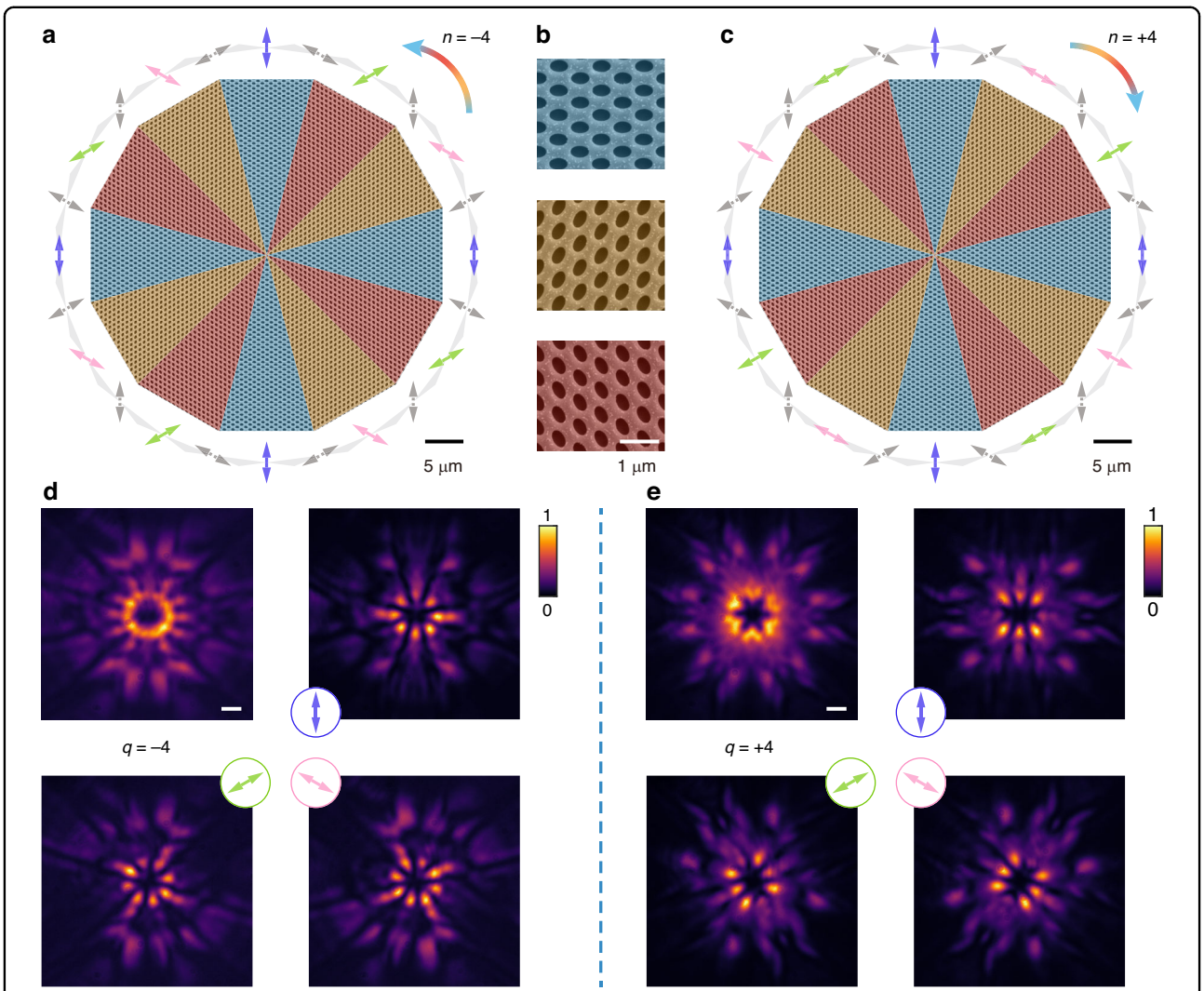

Fig. 4 Experimental realization of the compound cavities for corresponding vectorial lasing. **a**–**c** SEM images of the fabricated compound cavities for vectorial lasing with topological charge of −4 (**a**) and +4 (**c**). The colored arrows outside indicate polarization states of the composed q-BIC PhC slabs. Detailed SEM images of the composed q-BIC PhC slabs are shown in (**b**) with different colors highlighting the orientation of the elliptical holes. **d**, **e** Measured lasing images via the corresponding compound cavities. The colored arrows show the analyzed directions of applied linear polarizers. Scale bar, 1°

are provided in the Supplementary Information Section 11.

Distinct from previous topological cavity designs for vectorial lasing, such as the Dirac-vortex cavity, this methodology establishes a one-to-one correspondence between cavity design and lasing topological charge, offering unprecedented predictability in the design of vectorial lasing modes. The lasing mechanism in this work also differs from that in photonic disclination cavities. Disclination cavities utilize topological defect modes within the photonic bandgap, while our system designs topological lasing modes based on high-Q band-edge q-BICs. Our approach results in emission with pronounced directionality. More discussions on differences between the Dirac-vortex cavity, the photonic disclination cavity and the compound cavity in this work are provided in Supplementary Information Sections 13 and 14.

In conclusion, we have introduced a new topological concept of Möbius-like correspondence in q-BICs to construct the compound cavities supporting vectorial lasing with designable topological charges. Under symmetry breaking, the q-BIC with linear polarization evolves from the original high-order BIC with −2 topological charge in the triangular PhC slab, maintaining the high-Q property that favors lasing realization. Leveraging the unique properties of the Möbius-like correspondence, we propose a method for controlling topological charges of the compound cavity to achieve vectorial lasing. The

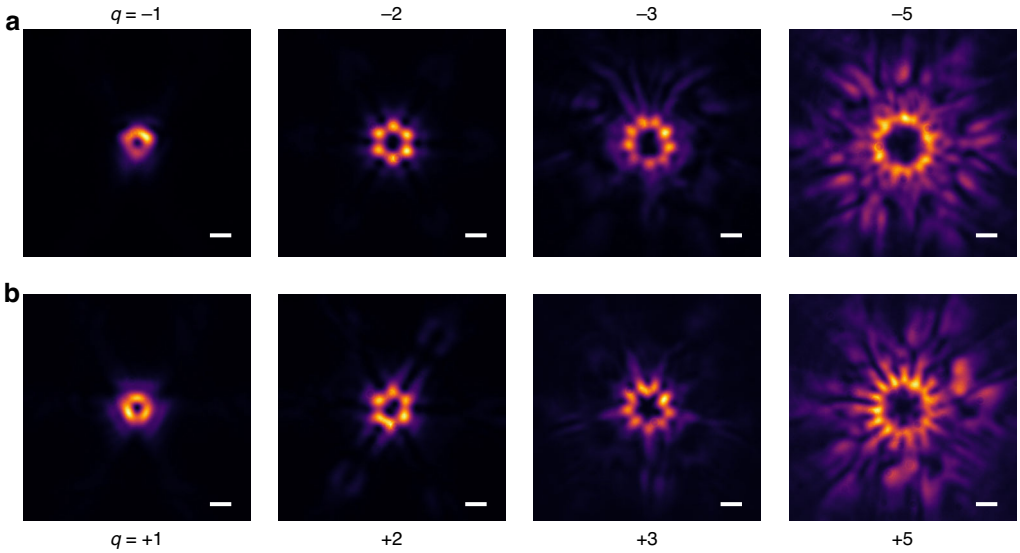

Fig. 5 Experimental realization of various vectorial lasing with different topological charges. **a**, **b** Measured lasing images with topological charges ranging from −1 to −3, −5 (**a**) and +1 to +3, +5 (**b**). The bright halos at the center correspond to vectorial lasing beams with different topological charges. Scale bar, 1°

designability of our method was confirmed through experimentally realized vectorial lasing with topological charges ranging from −5 to +5. Our work enables purposefully engineering lasing topological charges on an ultra-compact platform. Inspired by this work, future developments can explore generating other structured light profiles and applications of vectorial lasing in advanced optical communication, sensing, imaging, and next-generation compact photonic devices that leverage topological properties for enhanced performance.

Materials and methods

Simulations

Finite-element method (FEM) simulations were performed using COMSOL Multiphysics to obtain the photonic band structure, corresponding polarization distributions and modal profile of the lasing mode. For the simulations of the photonic band structure and corresponding polarization distributions, periodic boundary conditions were applied in the x and y directions, while the second-order scattering boundary condition was applied in the z direction. For the modal-profile simulations, the finite-size structure with second-order scattering boundary conditions was employed to simulate the field distribution ($|E|^2$) of the lasing mode. To evaluate the corresponding far-field profiles, the in-plane electric fields (E_x and E_y) of the lasing mode were sampled on a plane located about 1.5 wavelengths above the PhC structure, and the far-field intensity and polarization distributions were then obtained by performing a two-dimensional Fourier transformation of these fields.

Sample fabrication

The samples were fabricated on an optical silica substrate with a 140-nm-thick Si_3N_4 layer, deposited via a plasma-enhanced chemical vapor deposition (PECVD) system (Oxford PlasmaPro System 100). Standard nanofabrication techniques were utilized. A 320-nm-thick layer of CSAR 62 positive electron beam resist was spin-coated onto the Si_3N_4 layer and baked at 150 °C for 1 min, followed by a conductive polymer layer (AR-PC 5092.02). Electron beam lithography (JEOL JBX-8100FS) was performed at 100 kV and 2 nA, defining the specific patterns (period and orientation of elliptical holes) of the PhC structure on the resist layer. The unexposed resist served as a mask for subsequent reactive ion etching (RIE, Trion T2) using a mixture of CHF_3 and O_2 (the flow rates of these gases are 45 sccm:5 sccm). After etching, the remaining resist mask was removed via RIE with O_2 plasma (the flow rate is 50 sccm). Please see the Supplementary Information Section 2 for the schematic of the fabrication processes in this work.

Optical measurements

We implemented a momentum-space spectroscopy measurement system to carry out the optical measurements in the manuscript. Based on Fourier optics principles, the system enables analysis of momentum-space information and operates in two modes: spectrometer mode and imaging mode. In spectrometer mode, a spectrometer placed at the Fourier plane of the sample records in-plane momentum- and wavelength-resolved transmittance spectra. In imaging mode, a camera positioned at the Fourier plane captures laser beam profiles.

For the transmittance spectra measurements in spectrometer mode, we used a broadband white light source as the incident illumination. PL characterization was performed using a pulsed laser (wavelength: 800 nm; pulse width: ~100 fs; repetition rate: 1 kHz) to excite samples embedded with the gain medium IR-140-DMSO (5.3 mM concentration) at ambient temperature. These measurements were also conducted in spectrometer mode. By switching to imaging mode, we recorded the beam profiles of the vectorial lasing using a camera, with a linear polarizer introduced for polarization-analyzed measurements. For a schematic view and detailed descriptions of the optical setup, please refer to Supplementary Information Section 3.

Acknowledgements
This work was supported by National Key R&D Program of China (No. 2023YFA1406900 and No. 2022YFA1404800); National Natural Science Foundation of China (No. 12234007, No. 12321161645, No. 12221004, and No. 12404427); Major Program of National Natural Science Foundation of China (Grants No. T2394480, No. T2394481); Science and Technology Commission of Shanghai Municipality (22142200400, 21DZ1101500, 2019SHZDZX01, 23DZ2260100, and 24YF2702400). J.W. was further supported by the China National Postdoctoral Program for Innovative Talents (BX20230079) and the China Postdoctoral Science Foundation (2023M740721).

Author details
[1]State Key Laboratory of Surface Physics, Key Laboratory of Micro- and Nano-Photonic Structures (Ministry of Education) and Department of Physics, Fudan University, 200433 Shanghai, China. [2]Shanghai Research Center for Quantum Sciences, 201315 Shanghai, China. [3]Shanghai Key Laboratory of Metasurfaces for Light Manipulation, Fudan University, 200433 Shanghai, China. [4]Institute for Nanoelectronic Devices and Quantum Computing, Fudan University, 200438 Shanghai, China. [5]Collaborative Innovation Center of Advanced Microstructures, Nanjing University, 210093 Nanjing, China

Author contributions
J.W., L.S., and J.Z. conceived the basic idea and designed the experiments. J.W., X.W., and Z.W. gave the theoretical explanation and performed numerical simulations. X.W. and Z.W. fabricated samples. X.W. and J.W. constructed the measurement systems. X.W., Z.W., and J.W. performed the optical measurements. All authors analyzed the data. J.W. and X. W. wrote the manuscript, and all authors participated in discussions and revisions and approved the final version.

Data availability
We declare that all data needed to evaluate the conclusions are present in the paper and the Supplementary Information.

Conflict of interest
The authors declare no competing interests.

Supplementary information The online version contains supplementary material available at https://doi.org/10.1038/s41377-026-02269-7.

Received: 22 September 2025 Revised: 10 February 2026 Accepted: 3 March 2026
Published online: 30 March 2026

References

1. Zhan, Q. W. Cylindrical vector beams: from mathematical concepts to applications. *Adv. Opt. Photonics* **1**, 1–57 (2009).
2. Chen, J., Wan, C. H. & Zhan, Q. W. Vectorial optical fields: recent advances and future prospects. *Sci. Bull.* **63**, 54–74 (2018).
3. Shen, Y. J. et al. Optical vortices 30 years on: OAM manipulation from topological charge to multiple singularities. *Light Sci. Appl.* **8**, 90 (2019).
4. Forbes, A. Structured light from lasers. *Laser Photonics Rev.* **13**, 1900140 (2019).
5. Ni, J. C. et al. Multidimensional phase singularities in nanophotonics. *Science* **374**, eabj0039 (2021).
6. Forbes, A., de Oliveira, M. & Dennis, M. R. Structured light. *Nat. Photonics* **15**, 253–262 (2021).
7. Forbes, A., Mkhumbuza, L. & Feng, L. Orbital angular momentum lasers. *Nat. Rev. Phys.* **6**, 352–364 (2024).
8. Fang, L. et al. Vectorial Doppler metrology. *Nat. Commun.* **12**, 4186 (2021).
9. Dorn, R., Quabis, S. & Leuchs, G. Sharper focus for a radially polarized light beam. *Phys. Rev. Lett.* **91**, 233901 (2003).
10. Liu, M. et al. Super-resolution optical microscopy using cylindrical vector beams. *Nanophotonics* **11**, 3395–3420 (2022).
11. Parigi, V. et al. Storage and retrieval of vector beams of light in a multiple-degree-of-freedom quantum memory. *Nat. Commun.* **6**, 7706 (2015).
12. Ndagano, B. et al. Characterizing quantum channels with non-separable states of classical light. *Nat. Phys.* **13**, 397–402 (2017).
13. Sit, A. et al. High-dimensional intracity quantum cryptography with structured photons. *Optica* **4**, 1006–1010 (2017).
14. Sederberg, S. et al. Vectorized optoelectronic control and metrology in a semiconductor. *Nat. Photonics* **14**, 680–685 (2020).
15. El Ketara, M., Kobayashi, H. & Brasselet, E. Sensitive vectorial optomechanical footprint of light in soft condensed matter. *Nat. Photonics* **15**, 121–124 (2021).
16. Gao, X. M. et al. Dirac-vortex topological cavities. *Nat. Nanotechnol.* **15**, 1012–1018 (2020).
17. Yang, L. C. et al. Topological-cavity surface-emitting laser. *Nat. Photonics* **16**, 279–283 (2022).
18. Han, S. et al. Photonic Majorana quantum cascade laser with polarization-winding emission. *Nat. Commun.* **14**, 707 (2023).
19. Ma, J. W. et al. Room-temperature continuous-wave topological Dirac-vortex microcavity lasers on silicon. *Light Sci. Appl.* **12**, 255 (2023).
20. Hwang, M. S. et al. Vortex nanolaser based on a photonic disclination cavity. *Nat. Photonics* **18**, 286–293 (2024).
21. Shin, C. et al. Photonic disclination nanolaser with a high topological charge of 2. *ACS Photonics* **12**, 2530–2537 (2025).
22. Sroor, H. et al. High-purity orbital angular momentum states from a visible metasurface laser. *Nat. Photonics* **14**, 498–503 (2020).
23. Piccardo, M. et al. Vortex laser arrays with topological charge control and self-healing of defects. *Nat. Photonics* **16**, 359–365 (2022).
24. Ni, P. N. et al. Spin-decoupling of vertical cavity surface-emitting lasers with complete phase modulation using on-chip integrated Jones matrix metasurfaces. *Nat. Commun.* **13**, 7795 (2022).
25. Yang, Z. Q. Spin-momentum-locked edge mode for topological vortex lasing. *Phys. Rev. Lett.* **125**, 013903 (2020).
26. Miao, P. et al. Orbital angular momentum microlaser. *Science* **353**, 464–467 (2016).
27. Zhang, Z. F. et al. Tunable topological charge vortex microlaser. *Science* **368**, 760–763 (2020).
28. Chen, Y. et al. Observation of chiral emission enabled by collective guided resonances. *Nat. Nanotechnol.* **20**, 1205–1212 (2025).
29. Hsu, C. W. et al. Bound states in the continuum. *Nat. Rev. Mater.* **1**, 16048 (2016).
30. Kang, M. et al. Applications of bound states in the continuum in photonics. *Nat. Rev. Phys.* **5**, 659–678 (2023).
31. Huang, L. J. et al. Resonant leaky modes in all-dielectric metasystems: fundamentals and applications. *Phys. Rep.* **1008**, 1–66 (2023).
32. Wang, J. J. et al. Optical bound states in the continuum in periodic structures: mechanisms, effects, and applications. *Photonics Insights* **3**, R01 (2024).
33. Zhen, B. et al. Topological nature of optical bound states in the continuum. *Phys. Rev. Lett.* **113**, 257401 (2014).
34. Zhang, Y. W. et al. Observation of polarization vortices in momentum space. *Phys. Rev. Lett.* **120**, 186103 (2018).
35. Doeleman, H. M. et al. Experimental observation of a polarization vortex at an optical bound state in the continuum. *Nat. Photonics* **12**, 397–401 (2018).
36. Wang, B. et al. Generating optical vortex beams by momentum-space polarization vortices centred at bound states in the continuum. *Nat. Photonics* **14**, 623–628 (2020).
37. Rao, L. X. et al. Meron spin textures in momentum space spawning from bound states in the continuum. *Phys. Rev. Lett.* **135**, 026203 (2025).

38. Li, T. Y. et al. High-efficiency nonlocal reflection-type vortex beam generation based on bound states in the continuum. *Natl. Sci. Rev.* **10**, nwac234 (2023).
39. Tang, W. J. et al. Realizing high-efficiency third harmonic generation via accidental bound states in the continuum. *Opt. Lett.* **49**, 1169–1172 (2024).
40. Xiao, S. Y. et al. Polarization-controlled dynamically switchable high-harmonic generation from all-dielectric metasurfaces governed by dual bound states in the continuum. *Phys. Rev. B* **105**, 195440 (2022).
41. Liu, Z. J. et al. High-*Q* quasibound states in the continuum for nonlinear metasurfaces. *Phys. Rev. Lett.* **123**, 253901 (2019).
42. Koshelev, K. et al. Subwavelength dielectric resonators for nonlinear nanophotonics. *Science* **367**, 288–292 (2020).
43. Tonkaev, P. et al. Unconventional high-harmonic generation in resonant membrane metasurfaces. *Nat. Commun.* **16**, 11571 (2025).
44. Ardizzone, V. et al. Polariton Bose–Einstein condensate from a bound state in the continuum. *Nature* **605**, 447–452 (2022).
45. Gianfrate, A. et al. Reconfigurable quantum fluid molecules of bound states in the continuum. *Nat. Phys.* **20**, 61–67 (2024).
46. Kodigala, A. et al. Lasing action from photonic bound states in continuum. *Nature* **541**, 196–199 (2017).
47. Hwang, M. S. et al. Ultralow-threshold laser using super-bound states in the continuum. *Nat. Commun.* **12**, 4135 (2021).
48. Huang, C. et al. Ultrafast control of vortex microlasers. *Science* **367**, 1018–1021 (2020).
49. Sang, Y. G. et al. Topological polarization singular lasing with highly efficient radiation channel. *Nat. Commun.* **13**, 6485 (2022).
50. Chen, Y. et al. Compact spin-valley-locked perovskite emission. *Nat. Mater.* **22**, 1065–1070 (2023).
51. Wang, J. J. et al. Inherent spin-orbit locking in topological lasing via bound state in the continuum. *Phys. Rev. Lett.* **134**, 133802 (2025).
52. Cui, J. Y. et al. Ultracompact multibound-state-assisted flat-band lasers. *Nat. Photonics* **19**, 643–649 (2025).
53. Koshelev, K. et al. Asymmetric metasurfaces with high-*Q* resonances governed by bound states in the continuum. *Phys. Rev. Lett.* **121**, 193903 (2018).
54. Yoda, T. & Notomi, M. Generation and annihilation of topologically protected bound states in the continuum and circularly polarized states by symmetry breaking. *Phys. Rev. Lett.* **125**, 053902 (2020).
55. Wang, X. H. et al. Realizing tunable evolution of bound states in the continuum and circularly polarized points by symmetry breaking. *ACS Photonics* **10**, 2316–2322 (2023).